AGU PUBLICATIONS

Geophysical Research Letters

RESEARCH LETTER
10.1002/2014GL062266

Key Points:
- Capillary-driven microscale solute transport during drying
- Observation of a revers wicking effect

Correspondence to:
H. Ott,
Holger.Ott@shell.com

Citation:
Ott, H., M. Andrew, J. Snippe, and M. J. Blunt (2014), Microscale solute transport and precipitation in complex rock during drying, *Geophys. Res. Lett.*, *41*, 8369–8376, doi:10.1002/2014GL062266.

Received 23 OCT 2014
Accepted 14 NOV 2014
Accepted article online 18 NOV 2014
Published online 4 DEC 2014

This is an open access article under the terms of the Creative Commons Attribution-NonCommercial-NoDerivs License, which permits use and distribution in any medium, provided the original work is properly cited, the use is non-commercial and no modifications or adaptations are made.

Microscale solute transport and precipitation in complex rock during drying

Holger Ott[1,2], Matthew Andrew[2], Jeroen Snippe[1], and Martin J. Blunt[2]

[1]Shell Global Solutions International B.V., Rijswijk, Netherlands, [2]Department of Earth Science and Engineering, Imperial College London, London, UK

Abstract Formation drying and salt precipitation due to gas injection or production can have serious consequences for upstream operations in terms of injectivity and productivity. Recently, evidence has been found that the complexity of the pore space and microscopic capillary-driven solute transport plays a key role in the relationship between permeability and porosity. In this study, we investigate drying and salt precipitation due to supercritical CO_2 injection in single-porosity and multiporosity systems under near well-bore conditions. We image fluid saturation states and salt deposition by means of microcomputerized tomography scanning during desaturation. We observe capillary-driven transport of brine and the respective solutes on the pore scale. Solute transport between porosity classes determines the distribution of the deposits in the pore space and the permeability porosity relationships—$K(\phi)$—for flow-through drying.

1. Introduction

Drying of porous media is an important subject in many natural and industrial processes. During drying, water evaporates into a convective gas stream and the salts, originally dissolved in the brine, precipitate after reaching the solubility limit. It is known that salt precipitation can cause damage in historic monuments and buildings [see, e.g., *Goudies and Viles*, 1997; *Shahidzadeh-Bonn et al.*, 2010; *Flatt et al.*, 2014], controls water loss from land surfaces [*Chen*, 1992; *Scanlon et al.*, 1997; *Nachshon et al.*, 2011], and can lead to injectivity loss for gas production and injection operations like, e.g., for CO_2 storage [*Pruess and García*, 2002; *Fuller et al.*, 2006; *Giorgis et al.*, 2007] as the present work refers to. All these topics have the fundamental solute transport mechanisms in common, which makes it worthwhile to discuss solute transport and salt precipitation in porous media across disciplines. For the more general discussion, we refer to *gas* as the drying agent and to CO_2 in the more specific sections.

In contrast to most hydrogeological problems and oil and gas production scenarios, where flow is driven by viscous forces, in the drying regime brine saturations (S_W) are generally low and the brine phase is bound by capillary forces and hence largely immobile. In this regime, flow and solute transport is determined by capillary- and osmotic-driven processes. Resulting capillary pressure gradients are responsible for macroscopic solute transport, which determines the macroscopic distribution of the final salt deposit, and hence the porosity profile as a function of space, $\phi(x)$ [*Giorgis et al.*, 2007; *Ott et al.*, 2011]. However, as we will discuss in this paper, the associated permeability reduction and hence the $K(\phi)$ relationship is of microscopic origin and is determined by microscopic solute transport and eventually the exact microscopic distribution of the precipitate in the pore space [*Ott et al.*, 2011, 2013; *Roels et al.*, 2014; *Shokri*, 2014].

Recently, it has been pointed out that heterogeneity in the microscopic texture plays a fundamental role in controlling the water evaporation rate and the exact location of deposition (*Lehmann and Or* [2009]; *Nachshon et al.* [2011] in flow-over geometry and *Ott et al.* [2013] in flow-through geometry). For the flow-over case with—ideally—vertically continuous and connected macroporous and microporous regions, the microporosity acts like a wick [*Nachshon et al.*, 2011]. Without being in capillary contact, both subsystems would act according to the behavior of monomodal pore systems (described by *Coussot* [2000] and *Chauvet et al.* [2009]). If both subsystems are connected, i.e., aiming for capillary equilibrium, evaporation from the microporous system is compensated for by capillary-induced flow from the macroporous to the microporous system. Capillary-driven solute transport would as well be observed if the pore architecture were the same but the wettability of adjacent regions would be different. This issue has been recently discussed in *Shokri and Or* [2013]. For essentially water-wet systems, capillary pressure contrast

©2014. The Authors.

leads to an effectively higher "drying rate" of the macroporous system by flow [*Lehmann and Or*, 2009; *Nachshon et al.*, 2011]. As a consequence, salt precipitates preferentially in the fine-textured regions, i.e., the microporosity, while the coarse-textured regions sustain a high gas permeability [*Nachshon et al.*, 2011]. This is seemingly in contradiction to observations in flow-through geometry by *Ott et al.* [2013] as discussed in the following.

Ott et al. [2013] found for different pore systems a qualitatively different response of permeability to salt precipitation due to CO_2 injection. The effective permeability, $K_{\text{eff}} = k_{\text{rel}}(S_W) \times K$, increased during flow-through drying for a simple (essentially monomodal) sandstone, which implies that the relative gas permeability saturation function ($k_{\text{rel}}(S_W)$) increases due to drying—a reduction in water saturation—more rapidly than the decrease in absolute permeability ($K = K(\phi)$) due to salt precipitation. This limits the effect of salt precipitation on injectivity. It was suggested that salt does not precipitate in the CO_2 conducting channels and therefore does not contribute to a reduction in K_{eff} [*Ott et al.*, 2011, 2013]. However, for carbonates with a more complex pore architecture, K_{eff} decreased by orders of magnitude under comparable conditions [*Ott et al.*, 2013]. This result is in contrast to the sandstone case and can only be explained by precipitation of salt in the CO_2 conducting pore volume, which requires an active brine transport mechanism from smaller pores into the CO_2 conducting macroporosity.

With this study, we present direct observations of solute transport and precipitation in the rock's pore space during drying processes. The objective is to understand the distinctly different impact of salt precipitation on the injectivity in simple sandstone and in carbonates with a more complex pore architecture in flow-through geometry. For the carbonate case, we observe the brine transport from macroporous to the microporous regions suggested previously [*Lehmann and Or*, 2009; *Nachshon et al.*, 2011] and in a later stage a novel and seemingly counterintuitive reverse process, with brine flow into the larger pores. We explain both in a model of capillary equilibration processes. The data are directly relevant for the risk assessment of CO_2 storage operations with respect to injectivity, but the observed transport mechanisms are of general interest for other situations where salt precipitation occurs.

2. Microscale Experiments

We performed small-scale core flood experiments and used microcomputerized tomography (μCT) as an analytical tool for in situ pore-scale imaging of fluid phases and salt deposits. The samples were small in diameter (4 mm diameter and 20 mm length) in order to image at 2 μm voxel size and were mounted in a core holder; the assembly is reported in *Andrew et al.* [2014]. The core holder was vertically placed in a μCT scanner. CO_2 was injected from top to bottom using two displacement pumps operating in a constant pressure mode at the inlet and at constant retraction rate at the outlet.

The experiments were performed on Berea sandstone and Estaillades limestone. The two rock types are comparable in permeability and porosity—$\phi \approx 0.22$ versus 0.3 and $K \approx 500$ versus 200 mD for Berea and Estaillades—but represent a monomodal and a bimodal pore system, respectively. The rock characteristics are represented in the MICP (Mercury Injection Capillary Pressure) data shown in Figure 1. The limestone shows a characteristic step in the MICP corresponding to the invasion of the microporous volume, which is reflected in the two-peak structure in the pore-throat-size distribution. In this paper we refer to macroporosity as porosity that can be resolved by μCT scanning at the given resolution and to microporosity as porosity that we cannot resolve but that is visible in the gray scale behavior. Both samples show also porosity with pore sizes in between micro and macro, which we refer to as mesoporosity.

The rock samples were scanned in the dry state and subsequently saturated with KI-based brine by flooding with about 100 PV (pore volumes) at $T = 50°C$ and ambient pressure. We subsequently pressurized the fluid to 10 MPa and continued flooding for another few PV in order to remove dissolved air. We performed a μCT scan to verify full brine saturation ($S_W = 1$). Thereafter, supercritical (SC) CO_2 was injected at a flow rate of 0.12 mL/min (≈2 PV/min) representing realistic field rates near injection wells. We performed another μCT scan after injection of 100 PV CO_2. At this stage, there is typically no longer any viscous brine displacement and the cumulative water loss by evaporation is still negligible due to the low solubility of water in CO_2. In the following, we refer to this state as *after drainage*. The scan after drainage is the second reference point for data evaluation. From then on we continuously scanned the region of interest (≈2 mm diameter and 2 mm length in the center of the sample) under flow conditions with a time resolution of about 45 min. Continuous scanning allows the detection of any change in the rock-fluid system. We define the

©2014. The Authors.

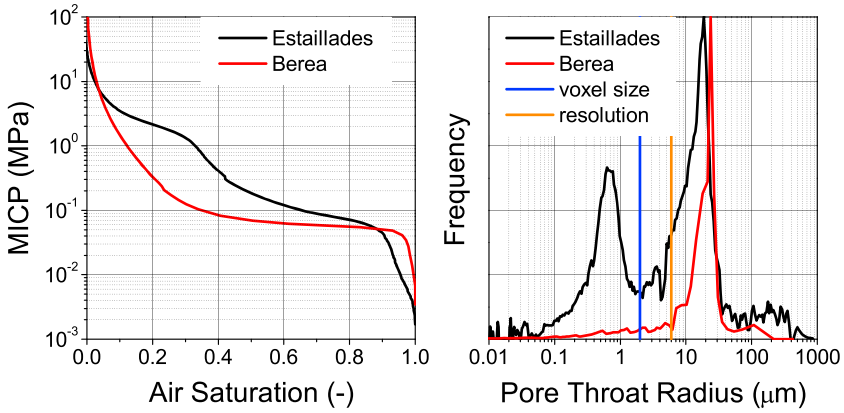

Figure 1. (left) Mercury Injection Capillary Pressure (MICP, micrometrics) curves of Berea sandstone and Estaillades limestone. (right) Pore-throat-size distributions of both rock types obtained from the MICP data. The blue and orange lines indicate the voxel size and the estimated physical resolution of the μCT scans.

time at which the μCT-determined sample state does not change any more as the time at which the sample is dry; the corresponding scan is used as third reference point for evaluation of the precipitated salt phase. We refer to this state as *after dry out*.

Figure 2 shows representative μCT cross sections recorded during the experiment on Berea sandstone. Figure 2a shows the typical rock structure in the dry state with macroporosity and mesoporous regions associated with feldspar and clay minerals, while Figure 2b shows the same image after drainage. Nonwetting CO_2 invades the pore space with the lowest entry pressure—the macroporosity. Finally, Figure 2c is an image after dry out about 10 h after drainage started. The locations of salt depositions are visible as bright spots. Salt precipitates essentially in the mesoporous regions that contained water at the end of drainage.

The data allow for two-phase segmentation of the volumes with the lowest X-ray attenuation (dark areas), corresponding to the macropore space in Figure 2a and the CO_2-saturated pore space in Figures 2b and 2c. The volumes were filtered (nonlocal means filter, Avizo fire, VSG) to reduce the noise level and registered (3-D image registration, Avizo fire, VSG) to account for small sample displacements during the experiment. We segmented by interactive thresholding (Avizo fire, VSG) and calculated the differences between the segmented macropore space and the segmented CO_2-saturated volumes in Figures 2b and 2c to extract the complementary brine and salt occupied macropore space after drainage and after dry out, respectively. Figures 2d and 2e show the segmented fluid phase after drainage. In Figure 2e, we additionally plot the salt phase in the macro pores after drying. It is evident that salt precipitated where the brine phase was after drainage. This is further illustrated in the 3-D images in the lower part of Figure 2, where the initial CO_2 percolation pathway and the total volume in which salt precipitated are shown. Both occupy complementary regions of the pore space.

We performed the same experiment under the same conditions on Estaillades limestone. Figure 3a shows μCT cross sections of the initially dry rock, the same cross section after brine saturation (S_W=1) Figure 3b and after drainage Figure 3c. Figures 3d and 3e were obtained during dry out after ≈24 h and after ≈7 d of CO_2 flooding, corresponding to about 3,000 and 20,000 PV CO_2.

Due to the high X-ray absorption coefficient of iodine, gray-scale changes are determined by salt migration only – i.e. solute transport – and other contributions can be neglected. In the following we speak of *depletion* when the gray-scale value decreases and of *enrichment* when the gray-scale value increases, corresponding to decreasing and increasing iodine concentration.

The early stage of the limestone (Estaillades) experiment shows similarities with the sandstone scenario: nonwetting CO_2 invades the macroporous regions. The remaining brine stays in the mesoporosity and in the microporous grains, as evidenced by the inverted gray scale contrast between solid and microporous grains compared to the dry scan. From Figures 3c and 3d we observe two trends: first, a salt depletion of the

©2014. The Authors.

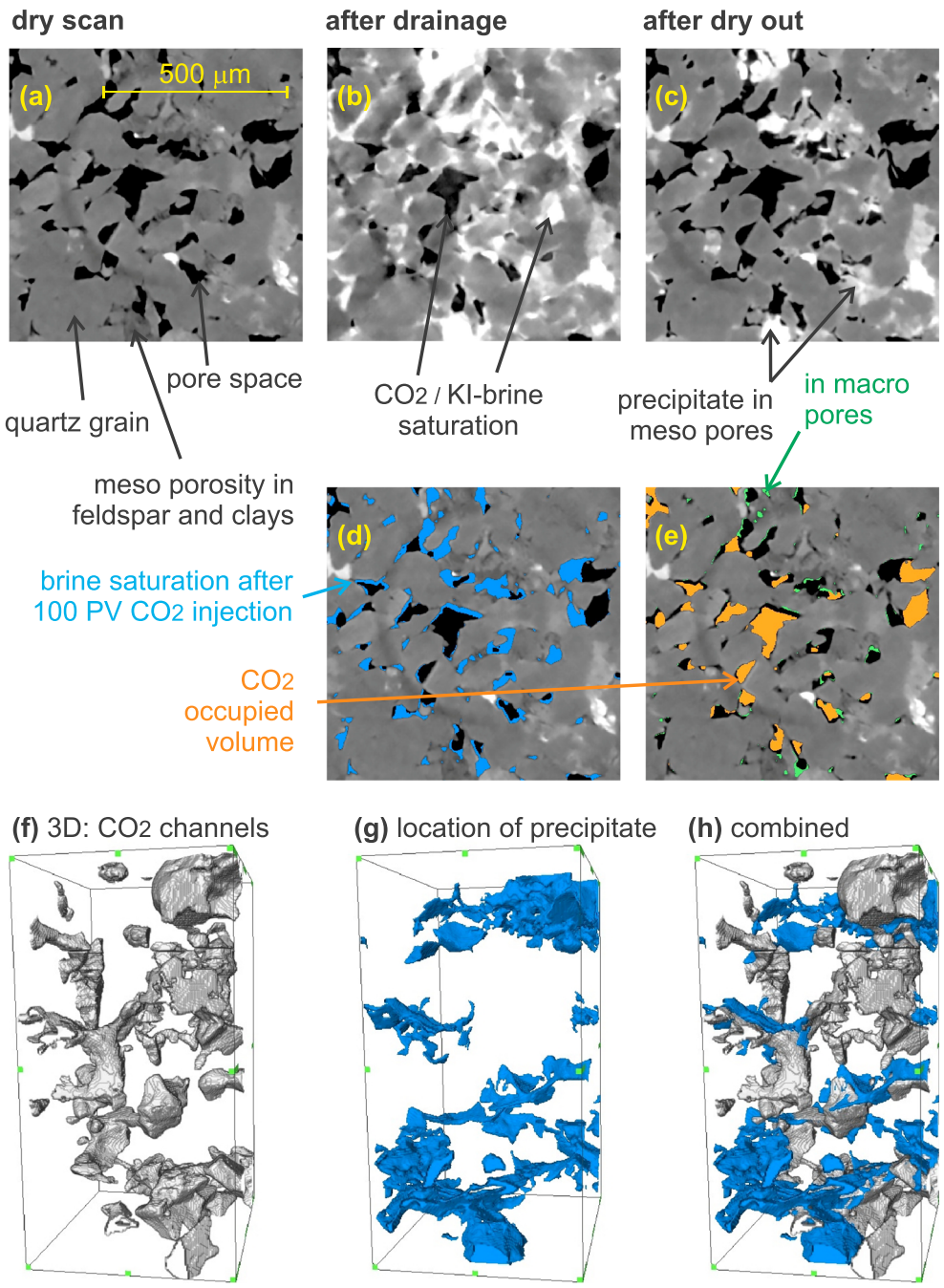

Figure 2. Microcomputerized tomography cross sections of Berea sandstone at different experimental stages: (a) in the dry state, (b) after presaturation and subsequent CO_2 drainage, and (c) after the experiment in the dry state. (d) The dry scan superimposed with the segmented brine phase after drainage (blue). (e) The complementary CO_2-occupied volume (orange) and the salt (green) in the macropores at a later experimental stage. (f) Segmented 3-D µCT volumes of the CO_2 percolation pathway after drainage, (g) the final precipitate, and (h) the both phases combined.

mesoporous regions and secondly, a salt enrichment in the microporous grains. To visualize the locations of depletion and enrichment, µCT images taken at different experimental times were subtracted. Before, contrast variation have been eliminated by linearly scaling the images, with the solid grains and the CO_2 phase occupied volumes as reference points on the gray scale. Figure 3f highlights the changes from Figures 3c to 3d; the orange/red color indicates depletion, while green/blue indicates enrichment of salt. There is obvious solute transport from the macroporous to the microporous system.

©2014. The Authors.

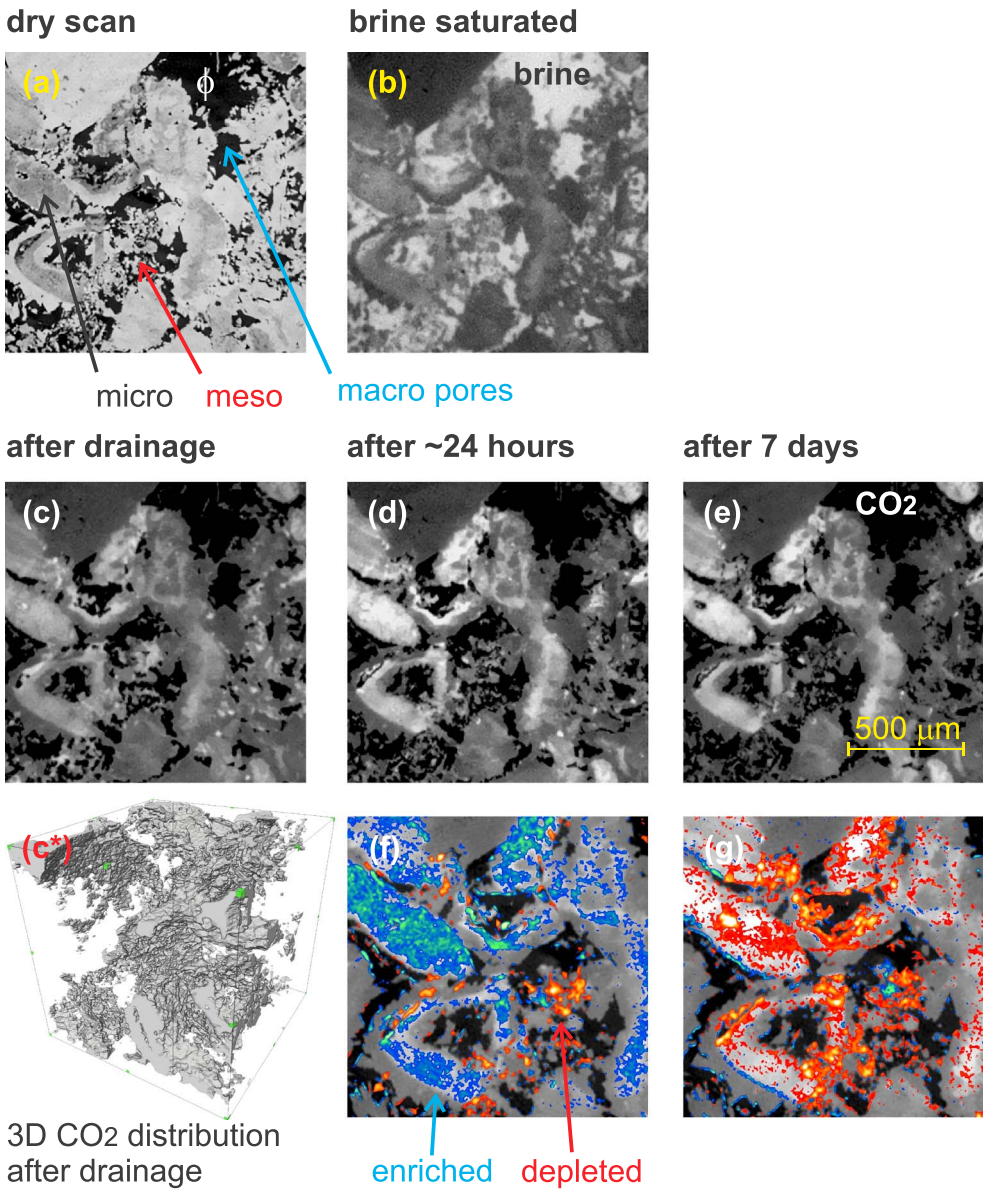

Figure 3. Microcomputerized tomography cross sections of Estaillades limestone at different experimental stages. (a) Initially dry sample, (b) after brine saturation, (c) after drainage, (d) after 24 h, and (e) after 7 days of CO_2 injection. (f and g) Zoom-ins of Figures 3d and 3e with the superimposed positive (enrichment) and negative (depletion) differences to the respective earlier time step. (c*) The 3-D CO_2 distribution after drainage.

In a later stage of the experiment the trend is reversed. Between Figures 3d and 3e there is a weak depletion of the microporous area which indicates reverse flow and which is shown in the same color coding in Figure 3g. It should be noted that the differences in Figures 3f and 3g are thresholded to highlight the locations of depletion and enrichment and not to quantify the concentrations. In the later stage there is a clear indication of solute transport from the microporous to the macroporous subsystem, which is counterintuitive and has not been observed before. Salt accumulates in the macropores potentially affecting the CO_2 transport.

3. Interpretation and Model

The data presented so far, together with a couple of simple arguments, allow the construction of a model that supports the findings of earlier work [*Ott et al.*, 2010, 2013]. We describe the model on basis of capillary

©2014. The Authors.

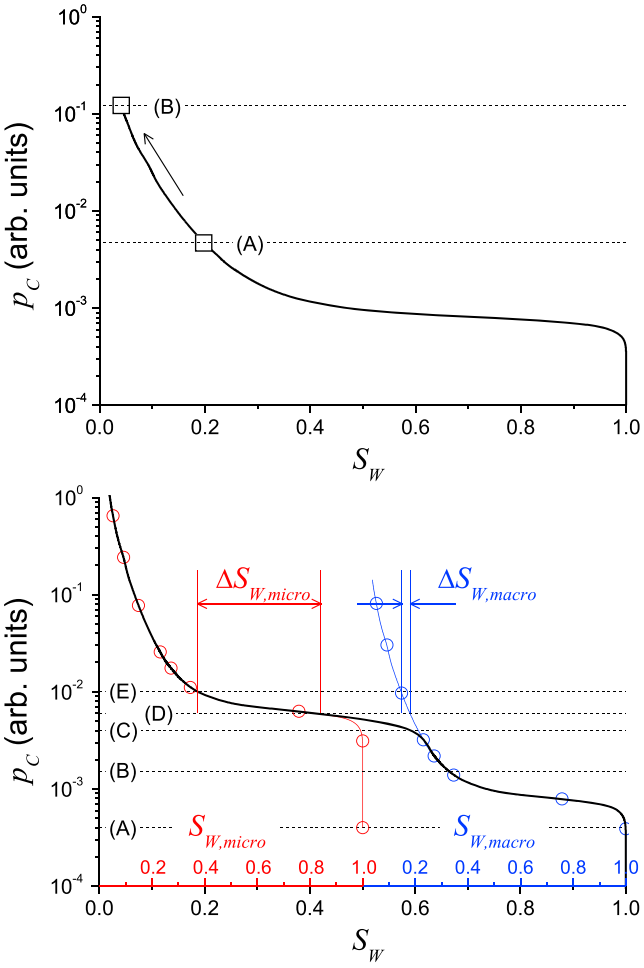

Figure 4. (top) The $p_C(S_W)$ curve of a simple sandstone (derived from MICP of Berea sandstone). (A) to (B) denote the p_C (p_C(A) and p_C(B)) and saturation change in the drying phase. (bottom) Constructed $p_C(S_W)$ curve of a dual-porosity system. The blue and red curves show decomposition into the macroporous and the microporous subsystem, respectively. (A) to (E) refer to capillary pressure levels during desaturation—p_C(A) to p_C(E) in the text.

equilibration as illustrated in Figure 4 and the diagrams in Figure 5, illustrating the flow and evaporation processes in a time sequence. We first discuss the monomodal sandstone case, which we describe with a single capillary pressure-saturation curve $p_C(S_W)$.

During the injection process, viscous brine displacement and water evaporation have been found to be dominant at different time scales. While residual brine saturation (p_C(A) in Figure 4) is usually reached after injection of a few PV, complete dry-out (p_C(B)) was reached after several hundred PV of injected gas. There is practically no viscous brine displacement during the drying process and precipitation, and the structure of the residually trapped brine phase is determined by capillary forces. After reaching the solubility limit, salt precipitates in the brine phase, and hence in the volume occupied by brine (Figure 5b). The brine-saturated volume retracts during evaporation, leaving the previously precipitated salt behind. During drainage there is no mechanism of brine transport and hence of solute transport into the gas-conducting volume. As a result, the effective permeability ($K_{\text{eff,CO2}} = K \times k_{r,\text{CO2}}$) can only increase over time, irrespective of absolute permeability reduction. Because of the separation of time scales of viscous displacement and evaporation, the maximum pore volume that can be filled by precipitate is the volume corresponding to the residual brine saturation after drainage, $S_{W,\text{res}}$ (illustrated in Figure 5b). We conclude that $S_{\text{salt,max}} = S_{W,\text{res}}$. In Berea sandstone $S_{W,\text{res}}$ is ≈0.2, which corresponds to the maximum observed salt accumulation due to capillary-driven countercurrent flow as reported in *Ott et al.* [2011].

These mechanisms hold as well for the more complex pore structure of carbonates. However, microporosity leads to additional effects influencing the location at which salt finally precipitates, and eventually the $K(\phi)$ relationship. While the monomodal sandstone case is described with a single p_C curve, we decompose the bimodal limestone in macroporous and microporous volumes with two individual p_C curves, as illustrated in Figure 4 (bottom). Both subsystems are assumed to be in contact with each other and are in capillary equilibrium during desaturation. The equilibrium states are represented by horizontal lines in Figure 4 and are denoted by (A) to (E), p_C(A) to p_C(E), respectively.

During primary drainage, gas invades only the macroporous system characterized by the lowest entry pressure (at p_C(A) in Figure 4) and the microporous volumes serve as brine reservoirs. If a microporous grain stays in contact with both, the residual brine phase of the macropores (mesopores) and the gas phase (at $p_C(B)$), the volume of water that evaporates gets refilled by the brine phase of the macroporous (mesoporous)

©2014. The Authors.

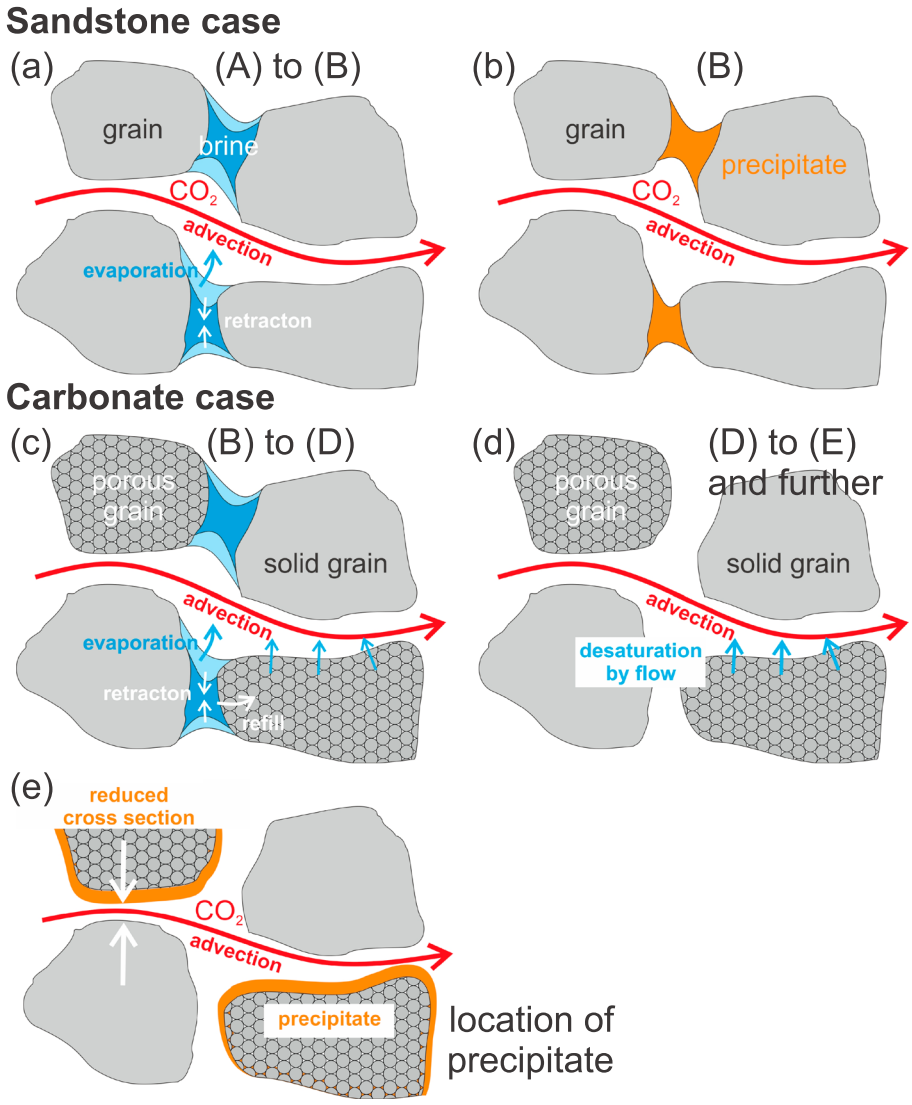

Figure 5. (a–e) Microscopic model of solute transport and salt precipitation for the sandstone case (top row) and the carbonate case. The intergranular porosity refers to macroporosity and the intragranular porosity to microporosity. The letters (A) to (E) refer to the respective capillary pressure levels in Figure 4.

system as illustrated in Figure 5c. Evaporation and refill lead to an effective increase of brine salinity in the micropores. This is by analogy to the dual-porosity effect in soils with brine transport from the macroporous to the microporous subsystem. Thus, it links to well-known physics but does not explain the earlier observation of K_{eff} reduction, which would require solute transport in the opposite direction, from the microporous regions to the gas-conducting channels. By further depletion of the macroporous (mesoporous) system, the brine supply to the microporous grains is no longer sufficient to prevent drying, and gas invades the microporous regions at p_C(C), which is illustrated in Figure 5d. This is equivalent to overcoming the entry pressure to the microporous system, but by water evaporation and not by viscous brine displacement. After exceeding the capillary entry pressure of the micropores, the brine flow is reversed; a small saturation change in the macropores $\Delta S_{W,\mathrm{macro}}$ (from p_C(D) to p_C(E); see Figure 4) will lead to a large saturation change $\Delta S_{W,\mathrm{micro}}$ associated with a substantial brine flow from the micro to the macroporous system to reach capillary equilibrium. A desaturation of the micropores by brine flow—and not by water vapor—leads to an effective solute transport to the gas-flow channels (the macroporous system) where salt precipitates. This finally leads to the very effective reduction of absolute and effective permeability (K and K_{eff}) compared to the rather mild impact observed in single modal sandstone.

©2014. The Authors.

4. Summary and Outlook

We have presented a comparative study of flow-through drying in simple and complex, i.e., monomodal and bimodal—pore space. Microcomputerized tomography scanning has been used to observe capillary-driven solute transport and salt precipitation directly and in situ. During the drying process, different transport regimes have been identified: (1) evaporation of a capillary-bound brine phase, (2) capillary equilibration by brine flow from the macroporous to the microporous subsystem and—seemingly counterintuitive—capillary equilibration by flow from the microporous to the macroporous subsystem and hence into the gas-transporting channels. The latter mechanism has been identified to reduce the effective permeability. We explained the findings by a simple model of capillary equilibration. The model qualitatively describes observations in earlier studies which show that for complex pore architectures there is a risk for injectivity loss during gas injection operations.

While the study explains the principal solute transport mechanisms, the observed time scales of drying are not captured in the model. The time scales are likely to be controlled by the exact configuration of the contact areas between the macroporous and microporous subsystems and the contact area with the drying agent. Potential sealing effects at boundaries that prevent further solute transport are also not yet understood and need further investigation.

Acknowledgments

The authors thank Steffen Berg and Saskia Roels for inspiring discussions and reviewing the manuscript and Ab Coorn for preparing the delicate small-scale samples. This work has been performed with support of the Qatar Carbonates and Carbon Storage Research Centre. Data are available upon request from the corresponding author (Holger.Ott@shell.com).

The Editor thanks Nima Shokri and an anonymous reviewer for their assistance in evaluating this paper.

References

Andrew, M., B. Bijeljic, and M. J. Blunt (2014), Pore-scale imaging of trapped supercritical carbon dioxide in sandstones and carbonates, *Int. J. Greenhouse Gas Control*, *22*, 1–14.

Chauvet, F., P. Duru, S. Geoffroy, and M. Prat (2009), Three periods of drying of a single square capillary tube, *Phys. Rev. Lett.*, *103*, 124502, doi:10.1103/PhysRevLett.103.124502.

Chen, X. Y. (1992), Evaporation from a salt-encrusted sediment surface: Field and laboratory studies, *Soil Phys. Hydrol.*, *30*, 428–442.

Coussot, P. (2000), Scaling approach of the convective drying of a porous medium, *Eur. Phys. J. B*, *15*, 557–566.

Flatt, R. J., F. Caruso, A. M. A. Sanchez, and G. W. Scherer (2014), Chemomechanics of salt damage in stone, *Nat. Commun.*, *5*, 4823, doi:10.1038/ncomms5823.

Fuller, R. C., J. H. Prevost, and M. Piri (2006), Three-phase equilibrium and partitioning calculations for CO_2 sequestration in saline aquifers, *J. Geophys. Res*, *111*, B06207, doi:10.1029/2005JB003618.

Giorgis, T., M. Carpita, and A. Battistelli (2007), 2D modeling of salt precipitation during the injection of dry CO_2 in a depleted gas reservoir, *Energy Conversion Manage.*, *48*, 1816–1826.

Goudies, A. S., and H. A. Viles (1997), *Salt Weathering Hazard*, Wiley, London.

Lehmann, P., and D. Or (2009), Evaporation and capillary coupling across vertical textural contrasts in porous media, *Phys. Rev. E*, *80*, 046,318, doi:10.1103/PhysRevE.80.046318.

Nachshon, U., N. Weisbrod, M. I. Dragila, and A. Grader (2011), Combined evaporation and salt precipitation in homogeneous and heterogeneous porous media, *Water Resour. Res.*, *47*, W03513, doi:10.1029/2010WR009677.

Ott, H., K. de Kloe, C. Taberner, F. Marcelis, Y. Wang, and A. Makurat (2010), Rock/fluid interaction by injection of supercritical CO_2/H_2S: Investigation of dry-zone formation near the injection well, paper presented at International Symposium of the Society of Core Analysis Conference Paper (SCA2010-20), Halifax, Nova Scotia, Canada, 4–7 October.

Ott, H., K. de Kloe, F. Marcelis, and A. Makurat (2011), Injection of supercritical CO_2 in brine saturated sandstone: Pattern formation during salt precipitation, *Energy Procedia*, *4*, 4425–4432.

Ott, H., J. Snippe, K. de Kloe, H. Husain, A. Abri, and A. Makurat (2013), Salt precipitation due to SC-gas injection: Single versus multi-porosity rocks, *Energy Procedia*, *37*, 3319–3330.

Pruess, K., and J. García (2002), Multiphase flow dynamics during CO_2 injection into saline aquifers, *Environ. Geol.*, *42*, 282–295.

Roels, S. M., H. Ott, and P. L. J. Zitha (2014), μ-CT analysis and numerical simulation of drying effects of CO_2 injection into brine-saturated porous media, *Int. J. Greenhouse Gas Control*, *27*, 146–154.

Scanlon, B. R., S. W. Tyler, and P. J. Wierenga (1997), Hydrologic issues in arid unsaturated systems and implications for contaminant transport, *Rev. Geophys.*, *35*(4), 461–490.

Shahidzadeh-Bonn, N., J. Desarnaud, F. Bertrand, X. Chateau, and D. Bonn (2010), Damage in porous media due to salt crystallization, *Phys. Rev. E*, *81*, 066,110, doi:10.1103/PhysRevE.81.066110.

Shokri, N. (2014), Pore-scale dynamics of salt transport and distribution in drying porous media, *Phys. Fluids*, *26*, 012,106, doi:10.1063/1.4861755.

Shokri, N., and D. Or (2013), Drying patterns of porous media containing wettability contrasts, *J. Colloid Interface Sci.*, *391*, 135–151.

©2014. The Authors.